

# Journal of Biomedical Optics

BiomedicalOptics.SPIEDigitalLibrary.org

## **Imaginary part-based correlation mapping optical coherence tomography for imaging of blood vessels *in vivo***

Chaoliang Chen  
Weisong Shi  
Wanrong Gao

# Imaginary part-based correlation mapping optical coherence tomography for imaging of blood vessels *in vivo*

Chaoliang Chen, Weisong Shi, and Wanrong Gao\*

Nanjing University of Science and Technology, Department of Optical Engineering, 200 Xiao Ling Wei, Nanjing, Jiangsu 210094, China

**Abstract.** We present an imaginary part-based correlation mapping optical coherence tomography (IMcmOCT) technique for *in vivo* blood vessels imaging. In the conventional correlation mapping optical coherence tomography (cmOCT) method, two adjacent frames of intensity-based structural images are correlated to extract blood flow information and the size of correlation window has to be increased to improve the signal-to-noise ratio of microcirculation maps, which may cause image blur and miss the small blood vessels. In the IMcmOCT method, the imaginary part of a depth-resolved complex analytic signal in two adjacent B-scans is correlated to reconstruct microcirculation maps. Both phantom and *in vivo* experiments were implemented to demonstrate that the proposed method can provide improved sensitivity for extracting blood flow information in small vessels. © 2015 Society of Photo-Optical Instrumentation Engineers (SPIE) [DOI: [10.1117/1.JBO.20.11.116009](https://doi.org/10.1117/1.JBO.20.11.116009)]

Keywords: optical coherence tomography; blood flow; sensitivity; signal-to-noise ratio.

Paper 150365RR received Jun. 7, 2015; accepted for publication Oct. 27, 2015; published online Nov. 30, 2015.

## 1 Introduction

Optical coherence tomography (OCT),<sup>1</sup> presented in 1991, is a very promising technique which is able to reconstruct three-dimensional (3-D) imaging of biological tissues noninvasively. Fourier domain OCT (FDOCT) was proposed by Fercher et al.,<sup>2</sup> and there are two forms of system setups: spectral-domain OCT (SDOCT)<sup>3-5</sup> and swept source OCT.<sup>3,4</sup> Compared with time domain OCT, FDOCT is of higher imaging speed and higher sensitivity for the imaging of tissue. After decades of development, FDOCT has been widely utilized in clinical applications.

The fact that nutrients and oxygen are transported to the entire body through blood suggests that information about the microcirculation maps in tissue is helpful for understanding and diagnosing diseases. A few types of extended functional FDOCTs have been developed to image microcirculation maps *in vivo* for the diagnosis of specific pathologies. For example, phase-resolved Doppler OCT (PRDOCT)<sup>6,7</sup> technology was developed to extract the velocity information of blood flow by evaluating the phase shift between two adjacent A-scans in an OCT B-scan frame. Although the PRDOCT method is of high resolution and high sensitivity to blood flow, its imaging performance is greatly deteriorated by at least two factors: (1) characteristic texture pattern artifacts, which are caused by the optical heterogeneity of the sample,<sup>8</sup> and (2) phase instability that is caused by the sample motion artifacts.<sup>9</sup> Furthermore, one of the limitations of the PRDOCT method is that the velocity of the particles moving in the direction perpendicular to the probe beam cannot be quantified. The optical angiography (OMAG) method<sup>10-12</sup> is another way to achieve imaging of blood perfusion by using heterodyne technology to separate the scattering signals caused by the moving scatters from the scattering signals caused by the static tissue background. This method directly analyzes and processes one B-scan image, which can minimize the phase instability noise caused

by the OCT system and sample. Recently, an ultrahigh-sensitive OMAG method,<sup>13</sup> in which the OMAG algorithm was performed in the C-scan direction, has been proposed to enhance the sensitivity for extracting blood flow information in small vessels. Another two recently developed high-contrast *in vivo* 3-D microcirculation imaging techniques are speckle-variance OCT (SVOCT) and phase-variance OCT (PVOCT). In the SVOCT method, blood flow information is extracted by analyzing the interline or interframe speckle variance of the intensity-based structural OCT images.<sup>14,15</sup> In intensity-based OCT structural images, the pixel values within the blood flow regions vary randomly over time, resulting in high variance, while the pixel values within the static tissue regions are constant, resulting in low variance. However, bulk tissue motions during *in vivo* experiments can increase the variance of pixel values within static tissue regions, resulting in noise in blood flow maps.<sup>14</sup> In the PVOCT method, the microcirculation maps are obtained by analyzing the variance of phase differences between consecutive B-scans at the same transverse position.<sup>16,17</sup> Compared with PRDOCT, the information about the blood flow perpendicular to probe beam can also be extracted by PVOCT.

Correlation mapping optical coherence tomography (cmOCT) was proposed by Jonathan et al.<sup>18</sup> to reconstruct microcirculation maps of a mouse brain *in vivo*. This method was then performed to reconstruct the microcirculation maps of a human volar forearm *in vivo* by Enfield et al.<sup>19</sup> Recently, the sensitivity for extracting the blood flow information within the deep tissue can be enhanced by a full-range spectral-domain cmOCT method,<sup>20</sup> in which the full-range spectral-domain OCT is used to increase the maximum imaging depth in tissue. A double cmOCT method<sup>21</sup> is presented to reconstruct the images of the subcutaneous microcirculation vascular network, and the spatial resolution of the spatial distribution of blood flow within the human skin can be improved.

\*Address all correspondence to: Wanrong Gao, E-mail: [wgao@njust.edu.cn](mailto:wgao@njust.edu.cn)

In a traditional cmOCT method, two adjacent frames of intensity-based structural OCT images are correlated to extract blood flow information, and the size of the correlation window has to be increased to improve the signal-to-noise ratio (SNR) of microcirculation maps, which may cause image blur and miss the images of small blood vessels. In this paper, we proposed an imaginary part-based correlation mapping optical coherence tomography method (IMcmOCT) to reconstruct microcirculation maps. Because the imaginary part of the depth-resolved complex analytic signal is more sensitive to motions than absolute values, resulting in an increase of the decorrelation degree of blood flow within tissue, the imaginary part-based images at the same lateral position are correlated to extract blood flow information in the proposed method. Both phantom and *in vivo* experiments were implemented to demonstrate that the proposed method can provide improved sensitivity for isolating a blood flow signal from static tissue background compared with traditional cmOCT.

## 2 Theory of the Proposed Method

Figure 1(a) is a block diagram for reconstructing microcirculation maps from spectral fringes detected by the SDOCT system with the IMcmOCT method. The DC component is first obtained by averaging all the spectral fringes into one B-scan, and then the new spectral fringes with the DC component subtracted are cubic-interpolated from the wavelength domain to the wavenumber domain to keep the axial resolution constant at different depths. After that, a complex analytic signal in the space domain can be obtained by performing Fourier transform on  $2\times$  zero-padded spectral fringes in the wavenumber domain. At this point, on one hand, the intensity-based structural image can be obtained by extracting the absolute value of the depth-resolved complex analytic signals, and the binary images can then be obtained by setting threshold values in structural images. The noise in the areas with no sample signal can be removed by overlapping binary images with correlation maps. On the other hand, the imaginary part-based images are correlated to extract blood flow information. Because the noise caused by motion artifacts due to cardiac and respiratory motions will occur in correlation maps, another two steps are necessary to compensate the motions before the correlation algorithm is performed. First,

the cross-correlation technique-based image registration is performed to compensate the integer pixel motions between the two local areas in two B-scans of imaginary part-based images, then the Kasai estimator is performed to compensate the axial sub-pixel phase shift between the A-scans in two local areas. Finally, the new imaginary part-based images are correlated to generate correlation maps, and blood flow maps can be obtained by overlaying the binary image with the correlation map.

Figure 1(b) shows the principle of cross-correlation technique-based image registration. This method can only compensate the integer pixel motions, because it aligns images by calculating the similarity measures with pixel values.<sup>22</sup> In OCT structural images, the distance interval between two adjacent pixels in the lateral direction is determined by the sampling frequency of the A-scans, while in the axial direction, the distance interval is determined by the parameters of the system hardware. However, the axial distance interval can be reduced by the zero-padding algorithm, so a  $2\times$  zero-padding technique was performed to decrease the distance interval by half,<sup>23</sup> resulting in an increase in the accuracy of image registration in the axial direction. It should be noted that the zero-padding algorithm is only a mathematical oversampling procedure and adds no more detailed information about tissue structure. In this work,  $x$ ,  $y$ , and  $z$  represent the Cartesian coordinates:  $x$  represents the fast scanning direction,  $y$  represents the slow scanning direction, and  $z$  represents the depth direction. In Fig. 1(b), the  $y$ 'th B-scan of an imaginary part-based image ( $I_y$ ) and the  $(y+1)$ 'th B-scan of the imaginary part-based image ( $I_{y+1}$ ) are correlated to generate a correlation map. Here,  $M$  is the lateral size of the correlation window and  $K$  is the pixel number of one A-scan in the depth direction. The local area with  $M$  pixels in the lateral direction and  $(K-2)$  pixels in the depth direction, marked by the red rectangle in  $I_y$ , is utilized as a kernel to calculate cross-correlation coefficients (XCCs) with the local area with  $(M+2)$  pixels in the lateral direction and  $K$  pixels in the depth direction marked by the red rectangle in  $I_{y+1}$ . Because the local area in  $I_{y+1}$  is larger than the kernel, there are 3 pixels of shifting range in both the lateral and depth directions. Let  $p$  and  $q$  denote the shifting pixel number in the lateral and depth directions, respectively, then XCCs can be expressed by

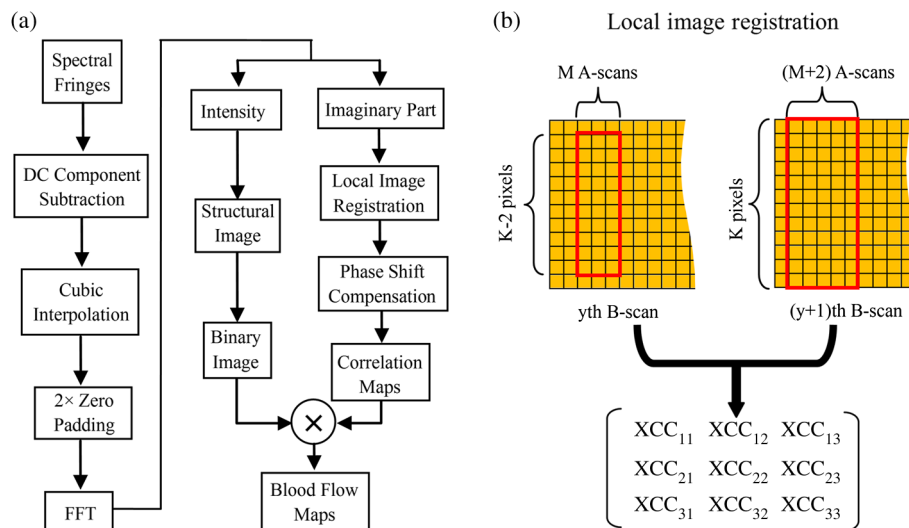


**Fig. 1** Theory of the proposed method. (a) The block diagram for reconstructing microcirculation maps from spectral fringes. (b) The process of cross-correlation technique-based image registration.

$$\text{XCC}(p, q) = \frac{\sum_{i=0}^{M-1} \sum_{j=1}^{K-2} [I_y(x+i+1, j+1) - \bar{I}_y][I_{y+1}(x+i+p-1, j+q-1) - \bar{I}_{y+1}]}{\sqrt{\sum_{i=0}^{M-1} \sum_{j=1}^{K-2} [I_y(x+i+1, j+1) - \bar{I}_y]^2} \sqrt{\sum_{i=0}^{M-1} \sum_{j=1}^{K-2} [I_{y+1}(x+i+p-1, j+q-1) - \bar{I}_{y+1}]^2}}, \quad (1)$$

$$p = 1, 2, 3 \quad \text{and} \quad q = 1, 2, 3,$$

where  $i$  and  $j$  are the pixel indices, and  $\bar{I}_y$  and  $\bar{I}_{y+1}$  represent the mean values of local areas. A  $3 \times 3$  matrix of XCCs can be obtained by Eq. (1), and the local area with the maximum value of the XCCs is correlated with the kernel in  $I_y$  to extract blood flow information.

Imaginary part-based images composed of amplitude and phase are correlated to extract the blood flow information in the IMcmOCT method. However, the phase signal is very sensitive to motions, so the axial subpixel phase shift has to be compensated to further suppress the noise caused by motion artifacts. The complex analytic signals in the two local areas aligned by the cross-correlation-based image registration method are marked as  $\tilde{\Gamma}_{y,\text{local}}$  and  $\tilde{\Gamma}_{y+1,\text{local}}$ , respectively. Then the Kasai algorithm is performed to estimate the mean phase shift in the axial direction

$$\bar{\phi} = \tan^{-1} \left[ \frac{\text{Im}\left\{ \sum_{i \in S} \sum_{j \in S} [\tilde{\Gamma}_{y,\text{local}}(i, j) \cdot \tilde{\Gamma}_{y+1,\text{local}}^*(i, j)] \right\}}{\text{Re}\left\{ \sum_{i \in S} \sum_{j \in S} [\tilde{\Gamma}_{y,\text{local}}(i, j) \cdot \tilde{\Gamma}_{y+1,\text{local}}^*(i, j)] \right\}} \right], \quad (2)$$

$$\text{cmOCT}_y(x, z) = \frac{\sum_{i=1}^M \sum_{j=0}^{N-1} [\Gamma_{x,y}(i, z+j) - \bar{\Gamma}_{x,y}][\Gamma_{x,y+1}(i, z+j) - \bar{\Gamma}_{x,y+1}]}{\sqrt{\sum_{i=1}^M \sum_{j=0}^{N-1} [\Gamma_{x,y}(i, z+j) - \bar{\Gamma}_{x,y}]^2} \sqrt{\sum_{i=1}^M \sum_{j=0}^{N-1} [\Gamma_{x,y+1}(i, z+j) - \bar{\Gamma}_{x,y+1}]^2}}, \quad (4)$$

where  $\bar{\Gamma}_{x,y}$  and  $\bar{\Gamma}_{x,y+1}$  represent the mean of the pixel values in the correlation window. The cross-sectional blood flow map can be obtained by shifting the kernel across the entire imaginary part image. Theoretically, the correlation values obtained by Eq. (4) are in the range from  $-1$  to  $1$ , with the value of  $0$  indicating weak correlation, and  $-1$  and  $1$  indicating strong anticorrelation and strong correlation, respectively.

For a stable SDOCT system, both the amplitude and phase of the depth-resolved complex analytic signal corresponding to blood flow regions are variables over time, while the amplitude and phase corresponding to static tissue regions are constant. For amplitude, those corresponding to blood flow regions vary randomly, resulting in a weak correlation degree, so two B-scans of intensity-based images are correlated to calculate the blood flow maps in the conventional cmOCT method. Because the velocity vector of moving red blood cells can be decomposed into an axial component (parallel to probe beam) and a transverse component (perpendicular to the probe beam), there are two cases when discussing the influence of moving red blood cells on phase: first, when the direction of the moving red blood cells is parallel to the probe beam, a linear phase shift can be caused because of the Doppler effect;<sup>6</sup> second, as we know, the average diameter of red blood cells is about  $10 \mu\text{m}$  and the displacement sensitivity of the phase is much smaller than the center wavelength of the light source in the

where  $S$  represents the local areas and  $\tilde{\Gamma}_{y+1,\text{local}}^*$  is the conjugate of  $\tilde{\Gamma}_{y+1,\text{local}}$ . The way to compensate the phase shift with the mean phase shift  $\bar{\phi}$  is given by

$$\tilde{\Gamma}'_{y+1,\text{local}} = \tilde{\Gamma}_{y+1,\text{local}} \cdot \exp(i\bar{\phi}), \quad (3)$$

where  $\tilde{\Gamma}'_{y+1,\text{local}}$  represents a new complex signal with the phase-shift compensated. Here,  $\Gamma_{x,y}$  and  $\Gamma_{x,y+1}$  are used to represent the imaginary parts of  $\tilde{\Gamma}_{y,\text{local}}$  and  $\tilde{\Gamma}'_{y+1,\text{local}}$ , respectively. At last, a correlation algorithm is performed to extract blood flow information. Assuming the size of the correlation window is  $M \times N$  pixels, the equation to calculate correlation maps can be given by

SDOCT system,<sup>24</sup> so phase perturbation can also be caused by the displacements of curve form of red blood cells when the direction of the moving red blood cells is perpendicular to the probe beam. Compared with the amplitude signal, the imaginary part consisting of amplitude and phase is more sensitive to motion. Therefore, the imaginary part instead of the amplitude is correlated to calculate blood flow maps in the

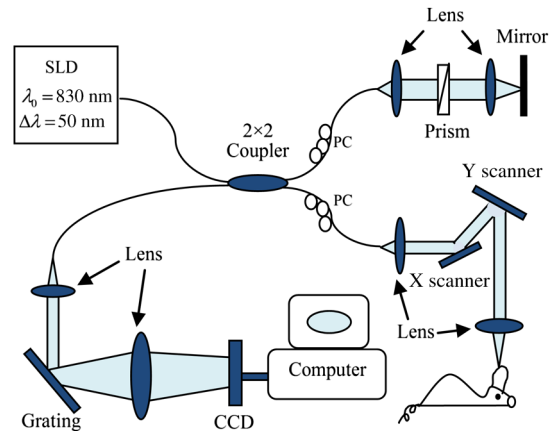


**Fig. 2** Schematic of spectral-domain OCT system used to collect the interference spectra to reconstruct the microcirculation maps. SLD, super luminescent diode; PC, the polarization controller; and CCD, the charge-coupled device.

IMcmOCT method, which can provide improved sensitivity for extracting blood flow information in small vessels. However, the noise due to cardiac and respiratory motions is also amplified, so cross-correlation technique-based image registration was performed to compensate the integer pixel motions, and the Kasai algorithm was performed to compensate the axial subpixel phase shift in the IMcmOCT method.

### 3 Experimental Results and Discussions

#### 3.1 System Setup

The system setup used to perform IMcmOCT is the same as the standard SDOCT system, and the schematic is shown in Fig. 2. The broadband light source is a super luminescent diode with a center wavelength of 830 nm and bandwidth of  $\sim 50$  nm, with a theoretical axial imaging resolution of  $\sim 6.1$   $\mu\text{m}$  in air. The reference arm contains a prism pair for dispersion compensation. In the sample arm, the beam is scanned in the  $x$ - and  $y$ -directions by using two scanning galvanometers. The driving signal of the galvanometers is generated by PCI-6733 (National Instruments). Light reflected back from the sample and reference arms is combined by the Michelson interferometer and sent to an imaging spectrometer consisting of a collimating lens, a diffraction grating, an achromatic focusing lens, and a

fast-line-scan CCD camera (2048 pixels,  $14 \times 14$   $\mu\text{m}^2$  pixel size). The spectral interference fringes are digitized at 16-bit resolution. Digitized spectral fringe profiles from the camera are acquired by a frame grabber card and transferred to a computer for further signal processing. The data acquisition and transfer are triggered by a signal generated by a computer synchronized with the ramp function that drives the  $x$ -direction scanning galvanometer.

In this work, the theoretical lateral resolution of the SDOCT is 6.4  $\mu\text{m}$ , and the frequency of A-scans was 33 kHz. In the  $x$ -direction, one-way scanning was performed, so a ramp function with a frequency of 16 Hz was used to drive the  $x$ -scanner, while a stepped ramp function was used to drive the  $y$ -scanner so that two consecutive B-scans at each position in the  $y$ -direction could be acquired. The sampling frequency of A-scans in the  $x$ -direction was 1000 A-scans within 2 mm, and in the  $y$ -direction, the scanner moved 300 steps within 1.5 mm and 600 B-scans were acquired.

#### 3.2 Results of Phantom Experiments

Three phantom experiments were implemented to demonstrate the improved performance of the IMcmOCT method. The sample is the flowing milk in a glass capillary with an inner diameter

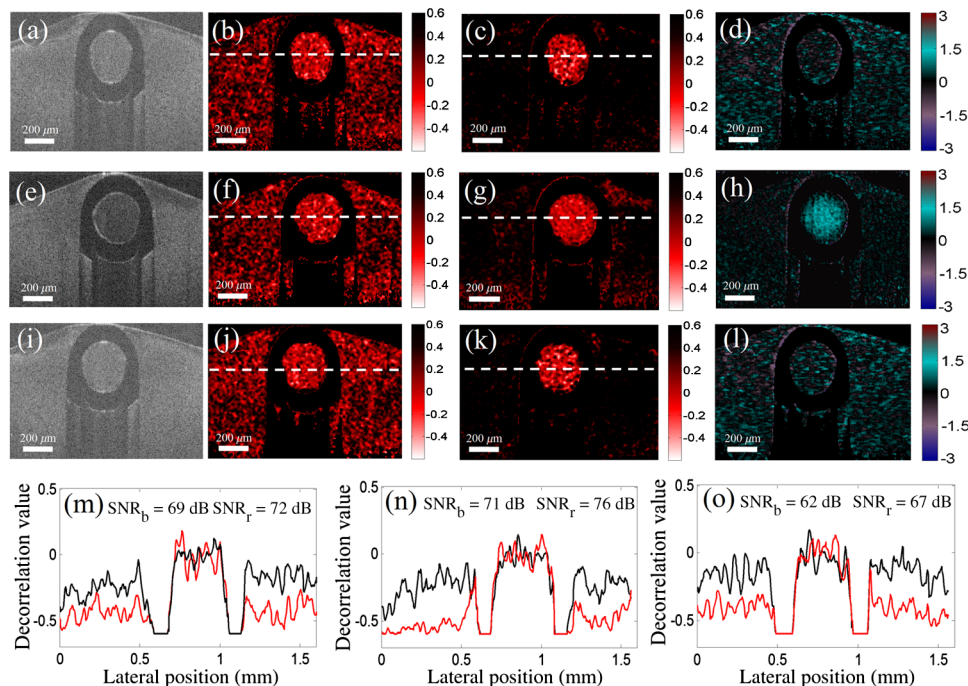


**Fig. 3** The results of phantom experiments. (a)–(d) The results under the condition that the capillary is mounted at an angle of  $\theta = 90$  deg, and the velocity of milk is 21.2 mm/s. (a) The structural image (b) and (c) are the correlation images obtained by the cmOCT method and IMcmOCT method, respectively. (d) The velocity image obtained by the PRDOCT method. (e)–(h) The results under the condition that the capillary is mounted at an angle of  $\theta = 81$  deg, and the velocity of milk is 21.2 mm/s. (e) The structural image (f) and (g) are the correlation maps obtained by the cmOCT method and IMcmOCT method, respectively. (h) The velocity image obtained by the PRDOCT method. (i)–(l) The results are under the condition that the capillary is mounted at an angle of  $\theta = 90$  deg, and the velocity of milk is 0 mm/s. (i) The structural images (j) and (k) are the correlation maps obtained by the cmOCT method and IMcmOCT method, respectively. (l) The velocity image obtained by the PRDOCT method. (m)–(o) Profiles of decorrelation values versus lateral position, black curve and red curve in (m) represent the data at the positions marked by the dashed white line in (b) and (c), respectively; black curve and red curve in (n) represent the data at the positions marked by the dashed white line in (f) and (g), respectively; and black curve and red curve in (o) represent the data at the positions marked by the dashed white line in (j) and (k), respectively.

of 300  $\mu\text{m}$  mounted in solid Agar. In three phantom experiments, the correlation window sizes of the conventional cmOCT method and the IMcmOCT method are all  $6 \times 3$  and  $6 \times 6$  pixels, respectively. In the first experiment, the velocity of the milk was 21.2 mm/s, which was controlled by a syringe pump, and the capillary is mounted at an angle of  $\theta = 90$  deg, resulting in the axial velocity component being zero. On this occasion, amplitude modulation and random phase perturbation

will be caused by the curved form of transverse moving scattering particles. The results are shown in Figs. 3(a)–3(d). Figure 3(a) is the structural image, and Figs. 3(b) and 3(c) are the correlation images obtained by conventional the cmOCT method and IMcmOCT method, respectively. Figure 3(d) is the Doppler image obtained by performing the PRDOCT algorithm on the same OCT dataset, and the algorithm can be expressed by

$$\Delta\phi(x, z) = \tan^{-1} \frac{\text{Im}\{\sum_{i=0}^{N-1} \sum_{j=0}^{M-1} [\tilde{\Gamma}(x+i, z+j) \cdot \tilde{\Gamma}^*(x+i+1, z+j)]\}}{\text{Re}\{\sum_{i=0}^{N-1} \sum_{j=0}^{M-1} [\tilde{\Gamma}(x+i, z+j) \cdot \tilde{\Gamma}^*(x+i+1, z+j)]\}}, \quad (5)$$

where  $\tilde{\Gamma}$  represents one B-scan of the complex analytic signal in the space domain,  $N$  and  $M$  represent the size of the averaging window, and  $\tilde{\Gamma}^*$  represents the conjugate of  $\tilde{\Gamma}$ . It can be found that the level of background noise in Fig. 3(c) is much lower than that in Fig. 3(b).

In the second experiment, the velocity of milk was also 21.2 mm/s, but the capillary was mounted at an angle of  $\theta = 81$  deg. In this case, amplitude modulation and phase shift will occur due to moving scattering particles. The results are shown in Figs. 3(e)–3(h). Figure 3(e) is the structural image. Figures 3(f) and 3(g) are correlation images obtained by the

cmOCT method and IMcmOCT method, respectively. Figure 3(h) is the Doppler image obtained by performing Eq. (5) on the same dataset. It can be found that the level of background noise in Fig. 3(g) is much lower than that in Fig. 3(f).

In the third experiment, the velocity of milk was 0 mm/s, and the capillary is mounted at an angle of  $\theta = 90$  deg. In this case, the milk is in Brownian motion, and both the amplitude perturbation and phase perturbation can be caused by randomly moving scattering particles. The results are shown in Figs. 3(i)–3(l). Figure 3(i) is the structural image. Figures 3(j)

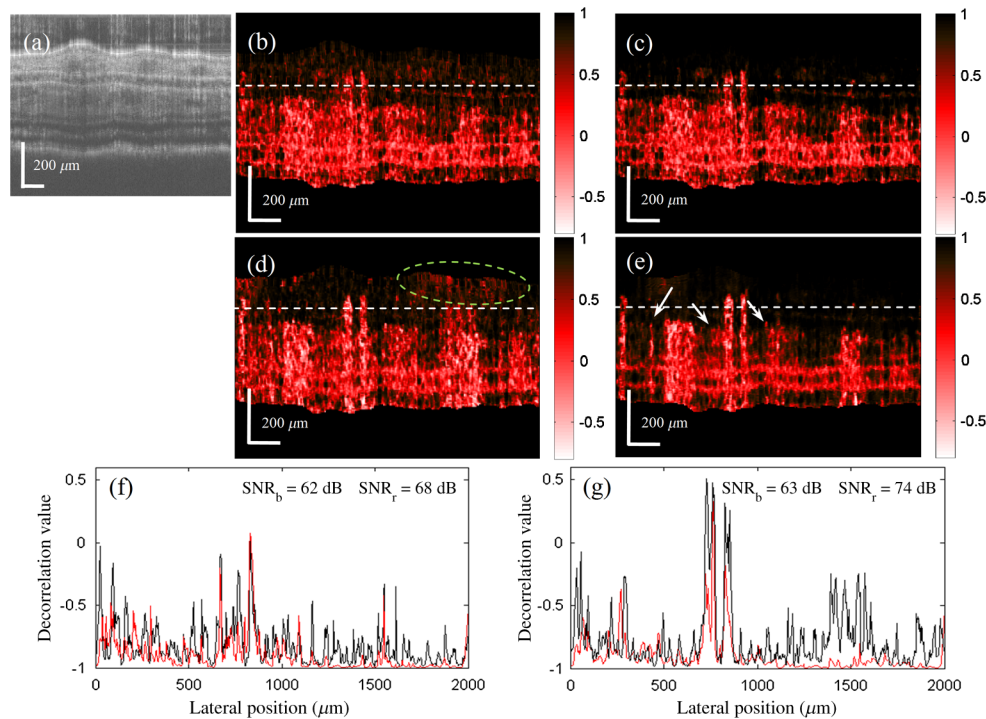


**Fig. 4** The cross-sectional maps at the position of  $y_0$  (marked by a red arrow in Fig. 6). (a) The structural image. (b and c) Blood vessel maps obtained by cmOCT method, but cross-correlation technique-based image registration is performed in (c). (d) The blood vessel map obtained by performing the cmOCT algorithm directly on imaginary part-based images. (e) The blood vessel map obtained by the IMcmOCT method, but the axial subpixel phase shift compensation algorithm is not performed. The signal marked by the dashed green ellipse in (d) is noise caused by motions. The signal marked by the white arrows in (e) represents blood vessels. (f) The profiles of the decorrelation values versus lateral position obtained by the cmOCT method, and the black curve with an SNR of 62 dB and red curve with an SNR of 68 dB represent the data at the positions marked by dashed white lines in (b) and (c), respectively. (g) The profiles of the decorrelation values versus lateral position obtained by the IMcmOCT method, and the black curve with an SNR of 63 dB and red curve with an SNR of 74 dB represent the data at the positions marked by dashed white lines in (d) and (e), respectively.

and 3(k) are the correlation images obtained by the cmOCT method and IMcmOCT method, respectively. Figure 3(l) is the Doppler image obtained by performing Eq. (5) on the same dataset. Compared with Fig. 3(j), the level of background noise in Fig. 3(k) is much lower.

Figures 3(m)–3(o) are the profiles of the correlation values with sign-inverted (decorrelation values) versus lateral positions in the three experiments. The black curve with an SNR of 69 dB and the red curve with an SNR of 72 dB in Fig. 3(m) represent the data at the positions marked by the dashed white line in Figs. 3(b) and 3(c), respectively. The black curve with an SNR of 71 dB and the red curve with an SNR of 76 dB in Fig. 3(n) represent the data at the positions marked by the dashed white line in Figs. 3(f) and 3(g), respectively. The black curve with an SNR of 62 dB and the red curve with an SNR of 67 dB in Fig. 3(o) represent the data at the positions marked by the dashed white line in Figs. 3(j) and 3(k), respectively. The way to calculate the SNR of the profiles in this work is the same as that in Ref. 9. All of the three plots quantitatively demonstrate that the proposed method can improve the SNR of microcirculation maps.

### 3.3 Results of In Vivo Experiments

An *in vivo* experiment was also implemented to demonstrate the improved sensitivity for isolating blood flow signal from static tissue background provided by the proposed method. A 3-D

OCT data set for a local region of  $1.5 \text{ mm} \times 2 \text{ mm}$  on a mouse ear was acquired with using  $600 \times 1000$  A-scans by the SDOCT system. In this experiment, the correlation window size of the conventional cmOCT method and IMcmOCT method is  $6 \times 3$  and  $6 \times 6$  pixels, respectively. The cross-sectional maps at the position of  $y_0$  (marked by a red arrow in Fig. 6) are shown in Fig. 4. Figure 4(a) is the structural image. Figures 4(b) and 4(c) are the blood vessel maps obtained by the conventional cmOCT method, but cross-correlation technique-based image registration is performed to remove the noise caused by motions in Fig. 4(c). Figure 4(d) is the blood vessel map obtained by directly performing the cmOCT algorithm on imaginary part-based images, and Fig. 4(e) is the blood vessel maps obtained by the IMcmOCT method, but axial subpixel phase shift compensation algorithm is not performed. The signal marked by the dashed green ellipse in Fig. 4(d) is the noise caused by motions. Comparing Fig. 4(b) with Fig. 4(c) and Fig. 4(d) with Fig. 4(e), it can be found that the cross-correlation technique-based image registration method is able to suppress the noise caused by integer pixel motions in both the cmOCT method and IMcmOCT method. The signals marked by the white arrows in Fig. 4(e) are blood flows, which is missed in the other three maps. Figure 4(f) shows the profiles of the decorrelation values versus lateral position obtained by the conventional cmOCT method, and the black curve with an SNR of 62 dB and the red curve with an SNR of 68 dB represent the data at the positions marked by the dashed white lines in Figs. 4(b) and 4(c), respectively. Figure 4(g)

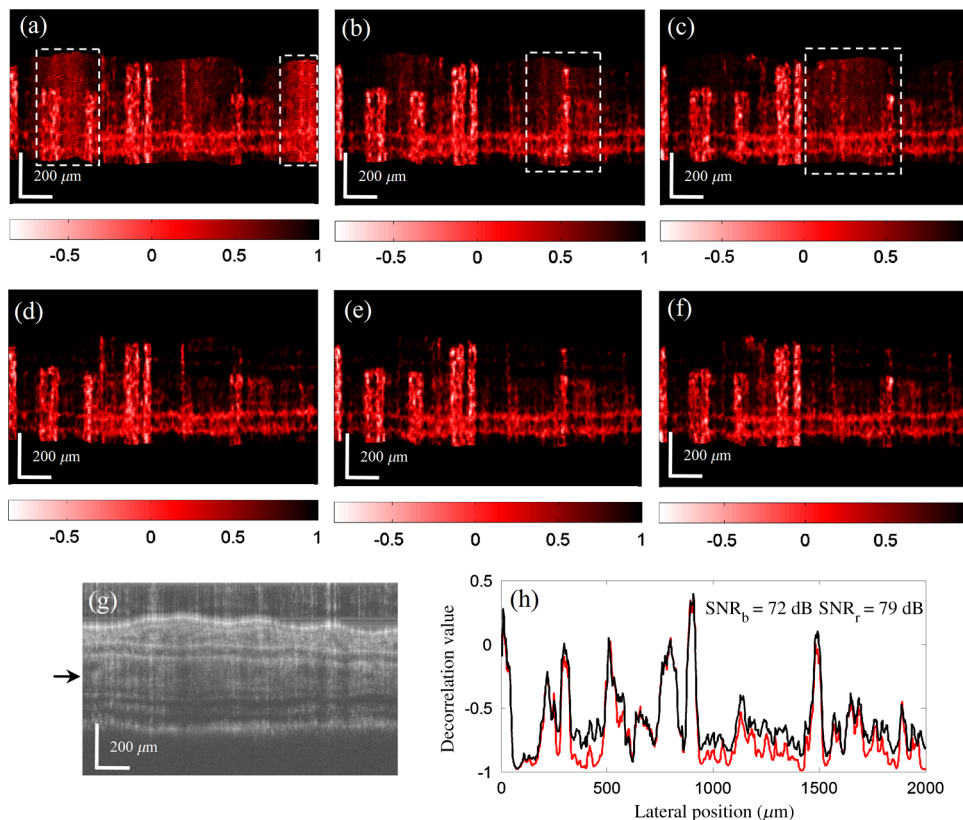


**Fig. 5** The three consecutive cross-sectional maps at the position of  $y_1$  (marked by a red arrow in Fig. 6). (a)–(f) Blood vessel maps obtained by the IMcmOCT method, but axial subpixel phase shift compensation algorithm is not performed in (a)–(c). (g) The structural image. (h) The profiles of decorrelation values versus lateral positions at the depth marked by a black arrow in (g), and black curve with an SNR of 72 dB and red curve with an SNR of 79 dB represent the data in the averaged images of (a)–(c) and (d)–(f), respectively.

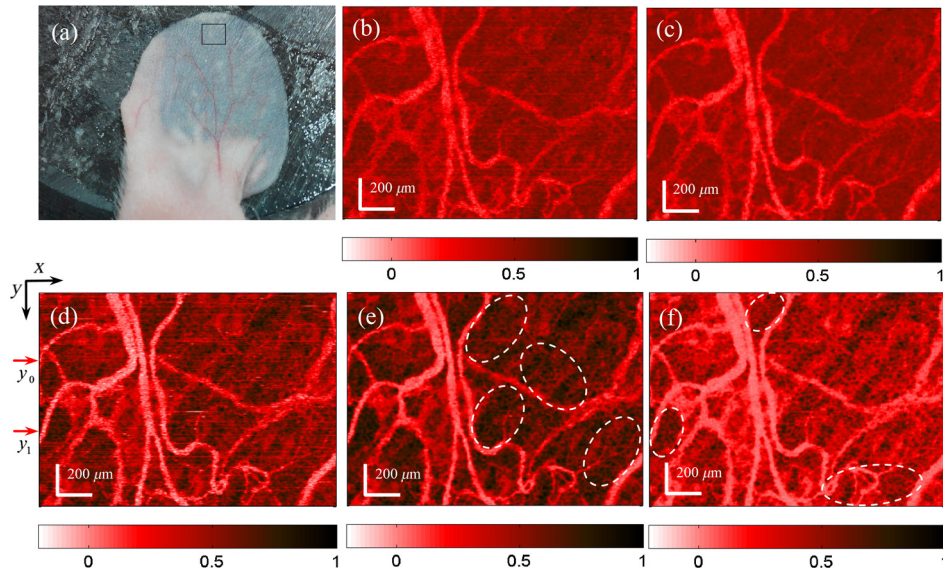


**Fig. 6** The *en face* MIP view images of the mouse ear. (a) The picture of a mouse ear and the local region marked by a black square ( $1.5 \text{ mm} \times 2 \text{ mm}$ ) was imaged with SDOCT. (b and c) Microcirculation maps obtained by the conventional cmOCT method, and the cross-correlation technique-based image registration is performed in (c). (d) The microcirculation map obtained by performing the cmOCT algorithm directly on imaginary part images. (e) and (f) The microcirculation maps obtained by the IMcmOCT method, but the axial subpixel phase shift is not compensated in (e). The positions  $y_0$  and  $y_1$  marked by red arrows in (d) indicate where the maps in Figs. 4 and 5 are located, respectively.

shows the profiles of the decorrelation values versus lateral position obtained by the IMcmOCT method, and the black curve with an SNR of 63 dB and the red curve with an SNR of 74 dB represent the data at the positions marked by the dashed white lines in Figs. 4(d) and 4(e), respectively. All the results demonstrate that the noise caused by integer pixel motions can be suppressed by the cross-correlation technique-based image registration method.

The three consecutive cross-sectional maps at the position of  $y_1$  (marked by a red arrow in Fig. 6) are shown in Fig. 5 to demonstrate that the noise caused by the axial subpixel phase shift can be suppressed by the mean Kasai estimator. Figures 5(a)–5(f) are blood vessel maps obtained by the IMcmOCT method, but the subphase shift compensation algorithm is not performed in Figs. 5(a)–5(c). Comparing Fig. 5(a) with Fig. 5(d), Fig. 5(b) with Fig. 5(e), and Fig. 5(c) with Fig. 5(f), it can be found that the noise in the regions marked by dashed white rectangles is effectively suppressed. Figure 5(g) is the structural image, Fig. 5(h) is the profiles of decorrelation values versus lateral positions at the depth marked by a black arrow in Fig. 5(g), the black curve represents the data in the average image of Figs. 5(a)–5(c), and the red curve represents the data in the average image of Figs. 5(d)–5(f). It can be found that the pixel values in blood flow regions on both curves are approximately equal to each other, but the noise level of the black curve is higher than that of red curve. The SNRs of the black curve and red curve are 72 and 79 dB, respectively.

The *en face* microcirculation maps of the mouse ear obtained by the maximum intensity projection algorithm are shown in Fig. 6. Figure 6(a) is the picture of the mouse ear, and the local region marked by a black rectangle was imaged with SDOCT. Figures 6(b) and 6(c) are microcirculation maps obtained by the conventional cmOCT method, but cross-correlation technique-based image registration is performed to remove the noise caused by motion artifacts in Fig. 6(c).

Figure 6(d) is the microcirculation map obtained by performing the cmOCT algorithm directly on imaginary part-based images. Figures 6(e) and 6(f) are the microcirculation maps obtained by IMcmOCT method, but the axial subpixel phase shift is not compensated in Fig. 6(e). The positions  $y_0$  and  $y_1$  marked by red arrows in Fig. 6(d) indicate where the maps in Figs. 4 and 5 are located, respectively. Comparing Fig. 6(b) with Fig. 6(c) and Fig. 6(d) with Fig. 6(e), respectively, it can be found that the cross-correlation technique-based image registration method is able to reduce the noise caused by integer pixel motions in both the cmOCT method and IMcmOCT method. Comparing Fig. 6(c) with Fig. 6(e), the blood flow in small vessels missed in Fig. 6(c) can be extracted in Fig. 6(e), such as those in the regions marked by dashed white ellipses, which demonstrates that the sensitivity for extracting blood flow information in small vessels can be improved by performing correlation algorithm on imaginary part-based images. Comparing Figs. 6(e) and 6(f), the blood flow in small vessels missed in Fig. 6(e) can be extracted in Fig. 6(f), such as those in the regions marked by dashed white ellipses in Fig. 6(f), which demonstrates that the SNR of microcirculation maps can be further improved by compensating the axial subpixel phase shift with a Kasai estimator. All results demonstrate that the proposed method can improve the sensitivity for extracting blood flow information in small vessels compared with a conventional cmOCT method.

## 4 Conclusion

In summary, we have presented an IMcmOCT method to reconstruct microcirculation maps *in vivo*. To our knowledge, the phase signal is first introduced in the cmOCT method to extract blood flow information. In this paper, the principle of the proposed method is presented in detail first, and then both phantom experiments and *in vivo* experiments were implemented to demonstrate that the proposed method can provide improved

sensitivity for extracting the blood flow information in small vessels and reconstruct the image of the small blood vessels, which is missed by the conventional cmOCT method.

### Acknowledgments

This research was supported by the National Natural Science Foundation of China (61275198 and 60978069). The study was approved by the Ethics Committee of Wuxi No. 3 People's Hospital.

### References

1. D. Huang et al., "Optical coherence tomography," *Science* **254**(5035), 1178–1181 (1991).
2. A. F. Fercher et al., "Measurement of intraocular distances by backscattering spectral interferometry," *Opt. Commun.* **117**(1), 43–48 (1995).
3. R. Leitgeb, C. Hitzenberger, and A. F. Fercher, "Performance of Fourier domain vs. time domain optical coherence tomography," *Opt. Express* **11**(8), 889–894 (2003).
4. M. Choma et al., "Sensitivity advantage of swept source, and Fourier domain optical coherence tomography," *Opt. Express* **11**(18), 2183–2189 (2003).
5. J. de Boer et al., "Improved signal-to-noise ratio in spectral-domain compared with time-domain optical coherence tomography," *Opt. Lett.* **28**(21), 2067–2069 (2003).
6. Y. Zhao et al., "Phase-resolved optical coherence tomography and optical Doppler tomography for imaging blood flow in human skin with fast scanning speed and high velocity sensitivity," *Opt. Lett.* **25**(2), 114–116 (2000).
7. Z. Ding et al., "Real-time phase-resolved optical coherence tomography and optical Doppler tomography," *Opt. Express* **10**(5), 236–245 (2002).
8. R. K. Wang and Z. H. Ma, "Real-time flow imaging by removing texture pattern artifacts in spectral-domain optical Doppler tomography," *Opt. Lett.* **31**(20), 3001–3003 (2006).
9. S. H. Yun et al., "Motion artifacts in optical coherence tomography with frequency-domain ranging," *Opt. Express* **12**(13), 2977–2998 (2004).
10. R. K. Wang et al., "Three dimensional optical angiography," *Opt. Express* **15**(7), 4083–4097 (2007).
11. R. K. Wang and L. An, "Doppler optical micro-angiography for volumetric imaging of vascular perfusion in vivo," *Opt. Express* **17**(11), 8926–8940 (2009).
12. L. An and R. K. Wang, "In vivo volumetric imaging of vascular perfusion within human retina and choroids with optical micro-angiography," *Opt. Express* **16**(15), 11438–11452 (2008).
13. L. An, J. Qin, and R. K. Wang, "Ultrasound sensitive optical microangiography for in vivo imaging of microcirculations within human skin tissue beds," *Opt. Express* **18**(8), 8220–8228 (2010).
14. A. Mariampillai et al., "Speckle variance detection of microvasculature using swept-source optical coherence tomography," *Opt. Lett.* **33**(13), 1530–1532 (2008).
15. A. Mariampillai et al., "Optimized speckle variance OCT imaging of microvasculature," *Opt. Lett.* **35**(8), 1257–1259 (2010).
16. J. Fingler et al., "Mobility and transverse flow visualization using phase variance contrast with spectral domain optical coherence tomography," *Opt. Express* **15**(20), 12636–12653 (2007).
17. D. Y. Kim et al., "In vivo volumetric imaging of human retinal circulation with phase-variance optical coherence tomography," *Biomed. Opt. Express* **2**(6), 1504–1513 (2011).
18. E. Jonathan, J. Enfield, and M. J. Leahy, "Correlation mapping method for generating microcirculation morphology from optical coherence tomography (OCT) intensity images," *J. Biophotonics* **4**(9), 583–587 (2011).
19. J. Enfield, E. Jonathan, and M. Leahy, "In vivo imaging of the microcirculation of the volar forearm using correlation mapping optical coherence tomography (cmOCT)," *Biomed. Opt. Express* **2**(5), 1184–1193 (2011).
20. H. M. Subhash and M. J. Leahy, "Microcirculation imaging based on full-range high-speed spectral domain correlation mapping optical coherence tomography," *J. Biomed. Opt.* **19**(2), 021103 (2014).
21. A. Doronin and I. Meglinski, "Imaging of subcutaneous microcirculation vascular network by double correlation optical coherence tomography," *Laser Photonics Rev.* **7**(5), 797–800 (2013).
22. D. L. G. Hill et al., "Medical image registration," *Phys. Med. Biol.* **46**(3), R1–R45 (2001).
23. Y. Huang et al., "Motion-compensated hand-held common-path Fourier-domain optical coherence tomography probe for image-guided intervention," *Biomed. Opt. Express* **3**(12), 3105–3118 (2012).
24. O. Sasaki and K. Takahashi, "Sinusoidal phase modulating interferometer using optical fibers for displacement measurement," *Appl. Opt.* **27**(19), 4139–4142 (1988).

**Chaoliang Chen** received his BS degrees in optics engineering from Nanjing University of Science and Technology in 2011, then continued studying for a PhD in optics engineering from Nanjing University of Science and Technology. His research topic is imaging microcirculation maps *in vivo*.

**Weisong Shi** received her BS degrees in optics engineering from Nanjing University of Science and Technology in 2015, then continued studying for a PhD in optics engineering from Nanjing University of Science and Technology. Her research topic is reconstructing microcirculation maps of tissue *in vivo*.

**Wanrong Gao** received his PhD degree from Xi'an Institute of Optics and Fine Mechanics in 1996. He worked as a visiting scientist in Prof. So's Lab in Massachusetts Institute of Technology from February, 2002 to February, 2003 and in Prof. Izatt's Lab in Duke University from March, 2011 to March, 2012. He conducts research on biomedical optics and spectroscopy in Nanjing University of Science and Technology.